Contrib Mineral Petrol (1989) 102:389–405

Contributions to Mineralogy and Petrology

Transformation of enstatite – diopside – jadeite pyroxenes to garnet

Tibor Gasparik
Mineral Physics Institute, ESS, State University of New York at Stony Brook, Stony Brook, New York 11794, USA

Abstract. The high-pressure stability of enstatite(En)-diopside(Di)-jadeite(Jd) pyroxenes has been investigated experimentally with a split-sphere anvil apparatus (USSA-2000). On the enstatite-pyrope join, the compositions of garnet coexisting with enstatite were determined at 100–165 kbar and 1450–1850° C. The results indicate complete solubility between enstatite and pyrope. In the system $CaO-MgO-Al_2O_3-SiO_2$ (CMAS), the compositions of coexisting pyroxenes and garnet were determined at 100–165 kbar and 1250–1750° C. At 157 kbar, 1650° C, garnet with the composition $En_{79}Di_{21}$ (mol%) forms on the En–Di join. In the system $Na_2O-MgO-Al_2O_3-SiO_2$ (NMAS), the compositions of coexisting pyroxenes and garnet were determined at 60–160 kbar and 1200–1850° C. On the En–Jd join, the first garnet has the composition $En_{48}Jd_{52}$ at 135 kbar, 1650° C, and $En_{53}Jd_{47}$ at 140 kbar, 1500° C. On the Di–Jd join, the first garnet with the composition $Di_{63}Jd_{37}$ forms around 170 kbar, 1650° C. In the En–Di–Jd system, the first appearance of garnet with the composition $En_{42}Di_9Jd_{49}$ is estimated at 133 kbar, 1650° C. The new pyroxene with the composition $NaMg_{0.5}Si_{2.5}O_6$ (NaPx) transforms to garnet at 154 kbar, 1650° C. The experimental results indicate that the transformation of a two-pyroxene assemblage to garnet and residual pyroxene in the En–Di–Jd system could occur at pressures consistent with the 400 km seismic discontinuity and in a pressure interval of 0–3 kbar.

Introduction

Two major discontinuities in the seismic velocity and density profiles of the earth's mantle at 400 km and 670 km depth could result from phase transitions in mantle olivine and its high-pressure polymorphs, providing the normative olivine content of the mantle is 40–60 percent (Sawamoto et al. 1984; Weidner 1986; Ito and Takahashi 1987). Such an olivine-rich mantle is suggested by the compositions of mantle xenoliths. On the other hand, the compositions of ordinary and carbonaceous chondrites, which should be representative of the bulk Earth composition, are substantially higher in silica content (Liu 1982; Anderson and Bass 1986).

Herzberg and O'Hara (1985) pointed out that the compositions of mantle xenoliths define a trend tracing the polybaric eutectoids or temperature minima determined experimentally. This suggests that the mantle xenoliths most likely are solidified eutectoid melts, and thus their composition should not be representative of the mantle. The compositions of the first melts generated at these eutectoids or temperature minima become increasingly olivine-rich with increasing pressure. For a chondritic Earth, the residues remaining after removal of these initial melts would become pyroxene-rich with increasing depth. Such residues would not have sufficient olivine to produce the observed discontinuities in seismic velocities.

An alternative explanation for the discontinuities could be phase transitions in pyroxenes and their high-pressure transformation products. At 400 km depth, such a transition can be expected to correspond to the transformation from pyroxene to garnet. However, unlike olivine, which is a relatively simple binary solution, both pyroxene and garnet can be complex multicomponent solutions. Consequently, the transition from pyroxene to garnet is likely to be gradual, in contrast to the seismic observations that require a sharp transition. For example, the pyroxene-garnet transition in the $MgO-Al_2O_3-SiO_2$ (MAS) system (e.g. Akaogi and Akimoto 1977) is sharp only for the pure enstatite; for the compositions on the enstatite-pyrope join, the transition occurs gradually over a range of pressures. Such problems have led others to propose that the discontinuities reflect abrupt chemical changes in the mantle (Liu 1982; Anderson and Bass 1986).

The purpose of this study is to explore the possibility that the 400 km discontinuity is caused by a sharp phase transition from pyroxene to garnet. To achieve this goal, experimental data on the high-pressure stability and transformation of enstatite-diopside-jadeite pyroxenes to garnet were obtained at pressures of 60–165 kbar and temperatures of 1200–1850° C.

The composition of mantle pyroxenes

Natural pyroxenes stable at the relatively low pressures of the earth's crust and shallow upper mantle can contain a large number of components. With increasing pressure, the solubility of some components decreases resulting in simplification of the pyroxene chemistry.

At pressures above 100 kbar, the content of tetrahedral aluminum in pyroxenes becomes negligible (Yamada and Takahashi 1984), which eliminates the Tschermak components – $(Ca, Mg, Fe)Al_2SiO_6$. In the stability field of stishovite at pressures above 90 kbar, the Eskola components – $(Ca, Mg, Fe)_{0.5}AlSi_2O_6$ also become negligible (Gasparik

1985; Irifune et al. 1986), because the molar volume of SiO_2 in pyroxene is much larger than the volume of stishovite. In this study, stishovite was often present in the experimental products, but the coexisting pyroxenes rarely showed any significant deviation from stoichiometry.

The Fe-content of mantle pyroxenes is low, because the Fe/(Fe+Mg) ratio of the Earth's mantle is only 0.1–0.2, and iron is partitioned least into pyroxenes. The recently identified $NaMg_{0.5}Si_{2.5}O_6$ component (Gasparik 1988) could be present in mantle pyroxenes, but requires unusual bulk compositions with an excess of sodium with respect to aluminum (Angel et al. 1988). That leaves only three major components necessary to consider in the composition of mantle pyroxenes: enstatite ($Mg_2Si_2O_6$), diopside ($CaMgSi_2O_6$) and jadeite ($NaAlSi_2O_6$).

The high-pressure apparatus

Most of the experimental work has been carried out with a uniaxial split-sphere anvil apparatus (USSA-2000) designed after a similar device at the Institute for Study of the Earth's Interior, Okayama University, Misasa, Japan (e.g. Ito and Takahashi 1987). Since this is one of the first studies performed with this high-pressure device, a detailed description of the apparatus is included (see also Remsberg et al. 1988).

The split-sphere anvil apparatus consists of a 2000-ton uniaxial press with a two-stage anvil system capable of achieving pressures above 200 kbar at temperatures in excess of 2000° C. The first-stage anvil system is a steel sphere split in six parts. The anvils are glued permanently into upper and lower guideblocks and enclose a cubic cavity, 60 mm on edge, which contains the second-stage anvil assembly. The lower guideblock can be removed from the press on a carriage to facilitate access to the second stage during preparation of an experiment.

The second stage is assembled outside the press and consists of eight tungsten carbide cubes, 32 mm on edge, separated by pyrophyllite gaskets, teflon back-up gaskets and balsa wood spacers. The cubes are truncated at one corner and enclose an octahedral cavity that holds the sample assembly. The sample assembly is an octahedron made of pyrophyllite or MgO. The second stage is electrically insulated from the first stage by phenolic sheets. Electrical insulation between the adjacent cubes is provided by teflon tape.

The sample assembly used in this study is shown in Fig. 1. The diagram is a cross-section through an MgO octahedron with an edge length of 10 mm. Heating is provided by a lanthanum chromite sleeve with molybdenum (TZM) rings on both ends for better contact. A zirconia sleeve outside the heater provides thermal insulation. The sample is placed in a metal capsule which is electrically insulated from the heater by an MgO sleeve. (Platinum capsules were usually used below 1700° C, and molybdenum capsules at higher temperatures.) Alumina ceramic rods fill the space above and below the capsule. One of these is a two-hole ceramic rod with a W3%Re/W25%Re thermocouple positioned axially. The contact for the two thermocouple wires in the sample assembly is provided by the capsule. The wires cross the heater at the cold end, and exit the assembly near the apexes of a triangular face. The wires are electrically insulated from the heater, the molybdenum ring and the WC anvil with alumina ceramic tubes placed in grooves carved out in one of the triangular faces of the octahedron. The remaining space is filled with zirconia cement. The thermocouple wires are taken completely out from the second-stage anvil assembly, and the reference junction is compensated to 0° C. The assembly (with or without the sample) is fired at 1000° C in argon for 1 h.

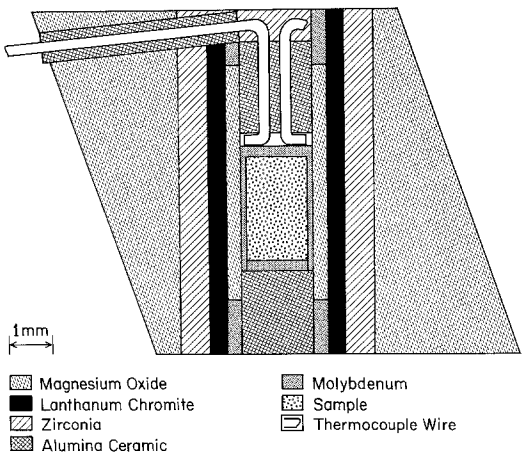

Fig. 1. The 10 mm sample assembly used in this study

Pressure calibration

The pressure calibration (Fig. 2) was carried out for the 10 mm MgO sample assembly and 5 mm truncations on the tungsten carbide cubes (Kennametal, grade KZ 313), with pyrophyllite and teflon gaskets 2.4 mm thick and 3.5 mm wide.

The sample pressure was calibrated against the press load at room temperature by monitoring the resistance change caused by the phase transitions in Bi I–II (25.5 kbar), Ba I–II (55 kbar), Bi III–V (77 kbar; Lloyd 1971), Ba II–III (126 kbar; Akimoto et al. 1975), ZnS (155 kbar; Block 1978) and GaAs (183 kbar; Suzuki et al. 1981). The high-temperature calibration was performed by reversing the coesite(Cs)-stishovite(St) phase transition at 1200° C (93 kbar) and at 1400° C (95 kbar; Yagi and Akimoto 1976). At higher pressures, the transition from enstatite to beta phase (Bt) and stishovite was located at 1400° C and 600 bar gauge pressure. The corresponding sample pressure of 165 kbar is consistent with the pressure scale of Sawamoto (1987). Based on this calibration (Fig. 2), V. Haniford (personal communication) located the forsterite-beta phase transition at 1400° C, 143 kbar, and at 1600° C, 152 kbar, in close agreement with Katsura (1988).

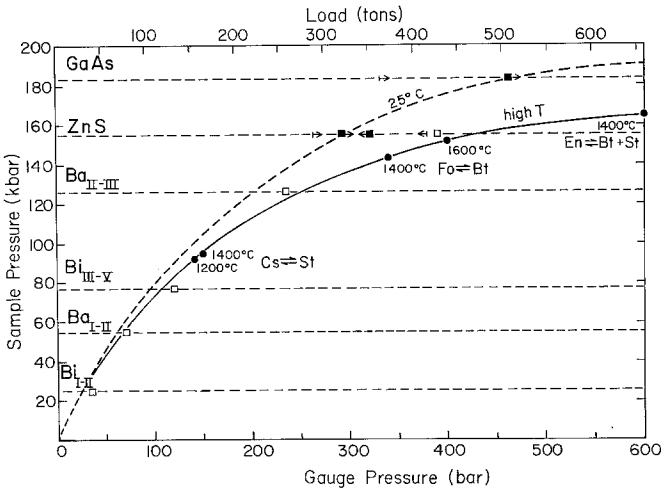

Fig. 2. Pressure calibration of the 10 mm sample assembly at room temperature (*dashed curve*) and high temperature (*solid curve*). *Open squares* are the room-temperature calibration results obtained with standard techniques; data points with *arrows* correspond to room-temperature calibration results obtained with the high-temperature assemblies. *Arrows* pointing to the right indicate transitions at the thermocouple junction, those pointing to the left indicate transitions in the center of the assembly. *Solid squares* represent the results obtained using calibrants mixed with AgCl. *Solid dots* correspond to the observations of the phase boundaries used for the high-temperature calibration

One set of calibration experiments at room temperature was performed with MgO octahedrons using standard techniques: for bismuth and barium, the calibrant wire was placed in the center of an octahedron between two MgO inserts with platinum strips for contact. A thin AgCl disc (2 mm × 0.2 mm) was placed under the calibrant wire to produce a sharp resistance change (Boyd and England 1960). For ZnS, the calibrant powder was placed between two copper wires 1.3 mm in diameter and 3.9 mm long. These calibration experiments gave results almost identical with the high-temperature calibration (see open squares in Fig. 2).

In the second set of calibration experiments at room temperature, the sample assembly was similar to the one used for the high-temperature work. The capsule was replaced with ZnS or GaAs powder, and the resistance change was monitored between the two thermocouple wires and between the wires and a platinum strip wrapped around the solid alumina rod. A section of the heater was replaced with a short MgO sleeve to prevent electricity flow through the heater. This arrangement allowed simultaneous pressure calibration at the center of the assembly and at the thermocouple junction (approximately 0.7 mm–0.8 mm off center). The data (shown in Fig. 2) demonstrate that pressure gradients within the sample assembly result in pressures at the thermocouple junction being up to 20 kbar higher than in the center. When the calibrant powders were mixed with AgCl, the pressure differences were reduced to less than 5 kbar. In this study, the presence of fluxes in the starting materials, used to enhance equilibration rates, also served to eliminate the pressure gradients in the samples.

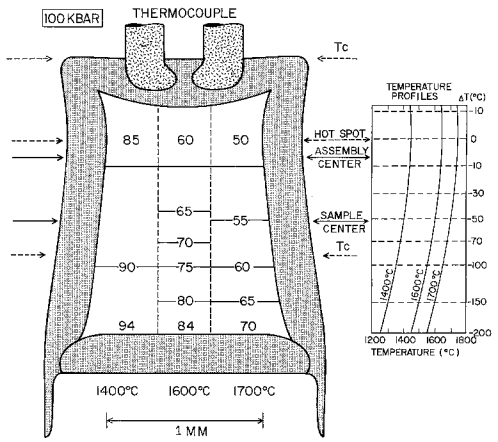

Fig. 3. Schematic cross-section of an experimental charge in the molybdenum capsule showing the distribution of compositions of the diopsidic pyroxene (in mol% diopside) coexisting with the enstatitic pyroxene in three samples at 100 kbar and 1400°, 1600° and 1700° C, and the corresponding temperature profiles. *Arrows* labeled *Tc* indicate nominal temperatures at the thermocouple junction and in the sample for a sample assembly with a symmetrical temperature distribution

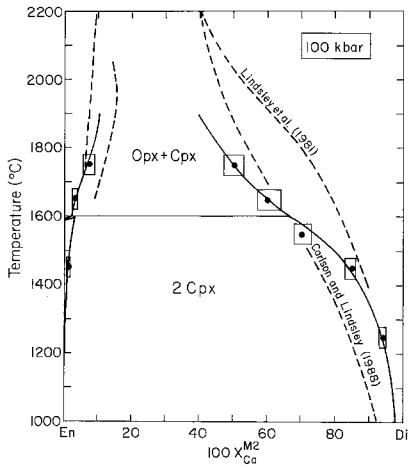

Fig. 4. Temperature-composition phase diagram for the enstatite-diopside join at 100 kbar (*solid lines*). Solid dots refer to the experimental observations discussed in text, with corresponding uncertainties indicated by the rectangles. *Dashed lines* are two-pyroxene solvi calculated with the solution models of Lindsley et al. (1981) and Carlson and Lindsley (1988)

Temperature calibration

Temperatures were measured with W3%Re/W25%Re thermocouples and controlled automatically. No correction for the effect of pressure on the thermocouple emf was applied. Occasional temperature fluctuations around the set point were typically only a few degrees and too rapid to affect the sample. A more important temperature correction arose from the temperature difference between the thermocouple junction (nominal temperature) and the hot spot (maximum temperature). This difference and the temperature distribution in the sample were estimated using the method of Takahashi et al. (1982). Their method, based on the solubility of enstatite in the diopsidic pyroxene coexisting with the enstatitic pyroxene, was modified to include the following improvements:

1. The experiments were extended to temperatures above 1500° C at which the solubility of enstatite in the diopsidic pyroxene is more sensitive to temperature.

2. Since the slope of the solvus at high pressures is not known very well, 3 experiments at 100 kbar and 1400, 1600 and 1700° C nominal temperatures were compared to correlate the compositions in the samples with the corresponding temperatures (Table 1, runs 192, 189, 197).

The compositions of the diopsidic pyroxene based on microprobe analyses of these three samples are shown schematically in Fig. 3. The compositions were transferred from the photomosaics of the samples containing the exact locations from which the microprobe analyses were taken. A wide band at the hot end of the samples shows minimal compositional variations, and corresponds to a region around the hot spot with a very low temperature gradient. The compositions in the hot spot of the sample at 1400° C are the same as the compositions in the cold end of the sample at 1600° C indicating that the temperature drop from the hot spot to the cold end in a sample is around 200° C.

The dashed arrows labeled Tc in Fig. 3 indicate the positions in the sample where the temperatures would be nominal, if the temperature distribution in the assembly were symmetrical with respect to the center of the assembly. However, the region around the hot spot showing minimal compositional variations is not centered around the center of the assembly, which indicates a slight asymmetricity in the temperature distribution. This is most likely the consequence of high thermal conductivity in the metal closure of the capsule, which places the nominal temperature closer to the center of the samples. The temperature profiles in Fig. 3 were constructed assuming that the center of the sample is at the nominal (thermocouple) temperature, and that the temperature difference between the hot spot and the cold end of the sample is 200° C. The temperature profiles and the pyroxene compositions indicate that the temperature difference between the hot spot and the center of the sample is around 50° C.

The temperature difference between the hot spot and the thermocouple junction was also measured directly with a thermocouple made of three wires and two junctions. For the distance of 0.73 mm between the two junctions measured after the experiment, the temperature difference at 1200° C was 50° C, which is consistent with the results based on the solubility of enstatite in the diopsidic pyroxene.

The phase relations on the enstatite-diopside join based on the calibration experiments are shown in Fig. 4. The compositions from the hot spot and the cold end of the sample were plotted for each experiment. Within the uncertainty of ±30° C, the data are consistent with a smooth solvus. The orthoenstatite(OEn)-clin-

Table 1. Conditions of equilibration experiments in the CMAS system and the average compositions of phases

Run #	Mix[a]	t[b] (h)	P_g[c] (bar)	P_s[d] (kbar)	T_s[e] (°C)	Phase[f]	An.[g]	Cations/6 oxygens					Sum
								Ca	Mg	Al	Si	Pb, V^{3+}	
Lead flux													
146	A	5.8	160	100	1450	Ga	51	0.159	1.404	0.903	1.540	0	4.006
					1250	Ga	18	0.169	1.376	0.931	1.529	0	4.005
					1450	Di	9	0.774	1.153	0.030	1.981	0.065	4.003
					1250	Di	3	0.844	1.034	0.029	1.985	0.108	4.000
					1450	En	7	0.015	1.988	0.008	1.992	0	4.003
130	A	7.0	320	140	1450	Ga	10	0.215	1.472	0.628	1.685	0	4.000
					1450	Di	5	0.866	1.039	0.014	1.994	0.086	3.999
					1450	En	2	0.003	1.989	0.004	2.002	0	3.998
135	A	7.0	320	140	1650	Ga	18	0.166	1.523	0.644	1.672	0	4.005
					1650	Di	11	0.754	1.177	0.016	1.986	0.073	4.006
					1450	Di	4	0.820	1.046	0.022	1.991	0.120	3.999
					1650	En	12	0.018	1.980	0.006	1.996	0	4.000
142	A	6.5	400	152	1450	Ga	24	0.245	1.578	0.386	1.799	0	4.008
					1250	Ga	6	0.294	1.518	0.430	1.771	0	4.013
					1450	Di	1	0.860	1.061	0.041	1.988	0.040	3.990
					1450	En	4	0.008	2.004	0.004	1.991	0	4.007
Vanadium flux[h]													
192	B	7.0	160	100	1450	Ga	26	0.183	1.413	0.830	1.559	0.028	4.013
					1250	Ga	11	0.209	1.365	0.848	1.539	0.050	4.011
					1450	Di	13	0.853	1.141	0.017	1.974	0.022	4.007
					1250	Di	14	0.940	1.051	0.010	1.975	0.028	4.004
					1450	En	4	0.014	2.005	0.005	1.987	0	4.011
189	B	7.0	160	100	1650	Ga	34	0.201	1.366	0.694	1.583	0.151	3.995
					1650	Di	34	0.590	1.310	0.035	1.981	0.057	3.973
					1450	Di	5	0.814	1.077	0.024	1.972	0.086	3.973
					1650	En	13	0.032	1.937	0.019	2.001	0	3.989
197	B	7.0	160	100	1750	Ga	10	0.185	1.396	0.746	1.584	0.089	4.000
					1750	Di	55	0.484	1.400	0.064	1.995	0.021	3.964
					1550	Di	18	0.692	1.233	0.035	1.972	0.052	3.984
					1750	En	31	0.071	1.870	0.050	1.992	0	3.983
427	B	6.0	190	110	1750	Ga	16	0.191	1.420	0.644	1.611	0.134	4.000
					1750	Di	22	0.540	1.381	0.043	1.971	0.047	3.982
					1550	Di	20	0.725	1.214	0.026	1.955	0.075	3.995
					1750	En	11	0.028	1.981	0.015	1.984	0	4.008
196	B	7.1	320	140	1450	Ga	48	0.279	1.462	0.475	1.719	0.073	4.008
					1250	Ga	24	0.325	1.368	0.545	1.670	0.099	4.007
					1450	Di	7	0.914	1.075	0.012	1.980	0.022	4.003
					1250	Di	7	0.956	1.043	0.006	1.988	0.012	4.005
					1450	En	5	0.007	2.002	0.003	1.993	0	4.005
193	B	6.7	320	140	1650	Ga	35	0.238	1.560	0.421	1.756	0.039	4.014
					1450	Ga	22	0.270	1.492	0.484	1.710	0.061	4.017
					1650	Di	3	0.925	1.110	0.006	1.974	0.004	4.019
					1450	Di	2	0.959	1.077	0.005	1.978	0	4.019
					1650	En	3	0.015	2.014	0.005	1.981	0	4.015
157	C	6.5	400	152	1450	Ga	26	0.299	1.481	0.438	1.771	0.013	4.002
					1450	Di	4	0.989	1.039	0.006	1.981	0	4.015
					1450	En	6	0.005	2.015	0.002	1.989	0	4.011
184	D	7.1	400	152	1650	Ga	44	0.275	1.585	0.257	1.830	0.063	4.010
					1450	Ga	23	0.296	1.534	0.305	1.780	0.101	4.016
					1650	Di	1	0.936	1.117	0.005	1.970	0	4.028
					1450	Di	4	0.960	1.075	0.005	1.979	0	4.019
					1650	En	5	0.016	2.016	0.002	1.982	0	4.016
182	D	6.4	460	157	1650	Ga	46	0.212	1.784	0.013	1.974	0.024	4.007
					1450	Ga	10	0.227	1.728	0.088	1.905	0.068	4.016
					1650	Di	11	0.914	1.116	0.003	1.983	0	4.016
					1450	Di	5	0.951	1.074	0.005	1.984	0	4.014
					1650	En	11	0.012	1.993	0.002	1.996	0	4.003

Table 1 (continued)

Run #	Mix[a]	t[b] (h)	P_g[c] (bar)	P_s[d] (kbar)	T_s[e] (°C)	Phase[f]	An.[g]	Cations/6 oxygens					Sum
								Ca	Mg	Al	Si	Pb, V^{3+}	
576	D	7.0	600	165	1650	Ga	14	0.190	1.813	0.020	1.976	0.010	4.009
					1450	Ga	3	0.231	1.785	0.009	1.976	0.012	4.013
					1650	Di	11	0.848	1.152	0.004	1.985	0.015	4.004
					1450	Di	5	0.911	1.075	0.005	1.996	0.011	3.998
					1650	En	6	0.025	1.975	0.001	1.999	0	4.000
					1450	En	6	0.012	1.985	0.001	2.000	0	3.998

[a] Bulk compositions of the mixes are given in Table 2
[b] Duration of experiments in hours
[c] Gauge pressure ($\times 1.096$ = load in metric tons)
[d] Sample pressure
[e] Sample temperature in the hot spot (nominal $T+50°$ C) and the cold end (nominal $T-150°$ C)
[f] In addition to the listed phases, assemblages include stishovite and melt
[g] The total number of analyses accepted from the given experiment for each phase
[h] Vanadium contents calculated from the weight deficiency in microprobe analyses with respect to an average of weight totals of enstatite from the same sample

Table 2. Compositions of starting materials (in moles)

Mix	SiO_2	MgO	$MgAl_2O_4$	$CaAl_2O_4$	$CaSiO_3$	$NaAlSiO_4$	$Na_2Si_2O_5$	PbO	PbF_2	V_2O_5	Seeds[a]
A	2.10	1.60	–	0.10	0.20	–	–	0.20	–	–	DEMPG
B	1.80	1.70	–	0.10	0.10	–	–	–	–	0.04	DEPG
C	2.00	1.70	–	–	0.30	–	–	–	–	0.10	DEPG
D	1.75	1.75	–	–	0.25	–	–	–	–	0.04	DEPG
E	1.10	1..00	–	–	–	–	–	0.05	0.05	–	EMP
F	1.70	1.40	–	–	–	0.30	0.20	–	–	–	JEM
G	1.75	1.50	–	–	–	0.25	0.10	–	–	–	JEM
H	1.40	0.80	–	–	–	0.60	0.10	–	–	–	JEM
I	1.85	1.70	–	–	–	0.15	0.20	–	–	–	EM
J	1.40	0.80	–	–	–	0.60	0.10	–	–	–	–
K	1.65	2.10	–	–	–	0.15	0.20	–	–	–	EP
L	2.70	3.40	–	–	–	0.30	–	–	–	–	M
M	1.00	–	0.40	–	–	0.60	–	0.10	0.10	–	JP
N	2.35	0.35	–	–	0.35	0.65	0.10	–	–	–	DJC
O	1.00	0.75	–	–	0.80	0.25	0.10	–	–	–	DJCM
P	1.00	0.60	–	–	0.65	0.40	0.10	–	–	–	DJCM
Q	1.50	0.50	–	–	–	–	0.50	–	–	–	–
R	1.80	1.40	–	–	–	–	0.20	–	–	–	DE
S	1.80	1.40	–	–	–	–	0.20	–	–	–	DEP
T	1.50	0.50	–	–	–	–	0.50	–	–	–	EP
U	1.50	0.50	–	–	–	–	0.50	–	–	–	P
V	1.75	1.75	–	–	0.25	–	0.10	–	–	–	Pig
W	2.30	0.50	–	–	–	0.80	0.70	–	–	–	JEP
X	1.80	1.50	–	0.10	–	–	0.30	–	–	–	DCEMG

[a] E=orthoenstatite, M=$En_{44}Py_{56}$ orthopyroxene, P=pyrope, G=grossular, D=diopside, J=jadeite, C=Ca-Tschermak pyroxene, Pig=$En_{80}Di_{20}$ pigeonite

oenstatite(CEn) transition was observed in the experiment at 1600° C nominal temperature (run 189): orthoenstatite at the boundary formed large (more than 100 μ) crystals poikilitically enclosing diopsidic pyroxene, in sharp contrast with much smaller (less than 50 μ) clinoenstatite in the cold half of the sample. The boundary was located in the center of the sample, thus at a temperature close to 1600° C. This boundary was also observed in the MAS system (run 535) at the same pressure and temperature. By comparing these observations with the orthoenstatite-clinoenstatite boundary of Pacalo and Gasparik (1989) in the pure $MgSiO_3$ system, it is concluded that the effect of calcium or aluminum in the enstatitic pyroxene on the boundary is very small.

Experimental techniques

Experiments in the split-sphere anvil apparatus started with a slow increase of pressure to the desired value (0.5–2 h, depending on the target pressure), after which the sample was heated to the desired temperature in a period of 10 min. The gauge pressure was maintained within 2 bars of the desired value, corresponding to an uncertainty of 0.6 kbar at 100 kbar sample pressure, and 0.1 kbar at 160 kbar sample pressure. Typical run durations were 6–7 h; experiments were terminated by shutting off power, causing the temperature to drop within a second. The pressure was then slowly decreased over a period of 2–3 h or more. The sample assem-

bly was removed from the apparatus and split along the axis of the cylindrical heater. The recovered capsule was then mounted for microprobe analysis; a polished mount contained a lengthwise section of the capsule with the sample. Wavelength dispersive analyses were obtained with a Cameca electron microprobe.

Starting materials (Table 2) were mechanical mixes made of ultrapure oxides and compounds (including a flux), to which large seed crystals (20–50 μ) of several different compositions were added in the amounts of 3 wt% each. The mix fully reacted in the press by the time the initial heating was completed and the desired run pressures and temperatures were reached. In the experiments quenched at this time, the experimental charge consisted of a fine matrix of crystals and glass with unchanged large seeds. The crystals in the matrix and any rims synthesized around the seeds, if present at all, were too fine to be analyzed by the electron microprobe.

During the course of an experiment, the seed crystals equilibrated with the surrounding crystalline phases and melt, approaching the equilibrium composition from the direction of their original composition. This usually happened by nucleating a new phase, which had a composition closer to the equilibrium composition than the original seed, on the surface of the seeds and slowly replacing them during the experiment. Under an optimal run duration, parts of the original seeds sufficiently large for microprobe analysis were replaced by a new phase, while corroded remnants of the original seeds were still preserved in the center of the new crystals. The compositions of these remnants identified the original seeds and thus the direction of the approach to equilibrium. Large portions of the newly-formed rims had compositions which showed limited variation, and were the closest to the equilibrium composition. Averages of these compositions are given in Tables. Small portions, often adjacent to the remnants, exhibited a wide range of compositions between the equilibrium and the original composition of the seeds. These compositions were included in the compositional fields shown in Figures. They indicate a unique path of the approach to equilibrium, and typically are not linear combinations of the equilibrium and the seed compositions.

It is emphasized that the rims around the seeds formed by slow replacement of the seed crystals under well defined experimental conditions, which were highly favorable for reaching equilibrium; these rims were not the result of synthesis from oxides during initial heating, which could potentially have produced metastable compositions. This was clearly demonstrated here in the study of the enstatite-pyrope join, performed with a starting material in which aluminum was present only in the pyrope and pyroxene seeds and not in the oxide mix. Any rims around the seeds formed by synthesis from oxides would have the pure enstatite composition instead of the observed compositions of the enstatite-rich garnet.

In a number of experiments in this study, the equilibrium composition was approached from two directions by using seeds of two different compositions. For example, the calcium content of the garnet coexisting with two pyroxenes in the CMAS system was reversed by approaching the equilibrium garnet composition from both pyrope and grossular seeds. Compositional fields produced by plotting all microprobe analyses separately for each kind of seed overlapped in the most equilibrated portions; the equilibrium composition is considered to be in the center of this overlap which may vary in size but most typically is 2–6 mol% wide. Thus, the equilibrium composition would not be a composition most distant from the original composition of a seed, but a composition 1%–3% closer to the original composition. This is important for the estimates of the equilibrium compositions in those experiments in which the equilibrium composition was approached from one direction only. Under a cautious interpretation, such experiments would qualify as dissolution experiments and thus would represent a half-bracket indicating the minimum solubilities. However, the experiments in which equilibrium compositions were reversed demonstrated that under the P–T conditions and run durations used in this study, equilibrium was most likely achieved.

Experimental results

The high-pressure stability of mantle pyroxenes was determined by experimental investigation of the following systems:

1. Enstatite – pyrope (MAS);
2. Enstatite – diopside – grossular – pyrope (CMAS);
3. Enstatite – jadeite – pyrope (NMAS);
4. Diopside – jadeite (NCMAS);
5. Enstatite – NaPx (NMS);
6. Enstatite – diopside – jadeite (NCMAS).

1 Enstatite – pyrope

Ringwood and Major (1966) first reported extensive solubility of pyroxene in garnet on the enstatite-pyrope join at pressures above 100 kbar; the phase relations on this join have been studied by Ringwood (1967), Akaogi and Akimoto (1977), Liu (1977) and Kanzaki (1987). These previous results are based mainly on synthesis experiments at temperatures around 1000° C. Garnet compositions were primarily determined by x-ray diffraction, although, some microprobe data were also reported. Akaogi et al. (1987) updated the results of Akaogi and Akimoto (1977), and in the proposed extrapolation to higher temperatures suggested that a complete solid solution of enstatite and pyrope exists above 1550° C. This is in conflict with the 2000° C experimental results of Sawamoto and Kohzaki (1985), which showed large immiscibility between the tetragonal garnet of the pure enstatite composition, or majorite (Mj – $Mg_4Si_4O_{12}$), and the majorite-rich cubic garnet. The stability of majorite was also reported by Kato and Kumazawa (1985).

In order to obtain additional constraints on the mixing properties of the majorite-pyrope garnet, particularly at higher temperatures, the solubility of enstatite in pyrope was determined at 100–165 kbar and 1450°–1850° C (Table 3). The starting material (Table 2) contained PbO – PbF_2 flux and seed crystals of synthetic pyrope, orthoenstatite and orthopyroxene with the composition $En_{44}Py_{56}$. In the course of the experiments, parts of the pyrope and aluminous pyroxene seeds were replaced with a new majorite-rich garnet phase whose composition approached the equilibrium compositions from the direction of the original composition of the seeds. Thus, it was possible to reverse those equilibrium compositions which were located between the pyrope and the aluminous pyroxene compositions (see Fig. 5). For the remaining experiments, the results represent the minimum solubilities of enstatite in garnet; however, the reversals at 125 and 140 kbar suggest that the experimental conditions in all experiments were favorable for reaching equilibrium.

Figure 5 shows the results at 1650° C. Electron microprobe analyses were obtained at 15 kV accelerating potential and 25 nA beam current using natural enstatite and grossular for standards. The garnet analyses from the hot spot and the cold end of the samples indicate that the temperature dependence of the enstatite solubility in garnet is small. The garnet analyses span the range of 1–100 mol% pyrope, confirming the prediction of Akaogi et al. (1987) that the solubility of enstatite in garnet is complete at these high temperatures.

The mixing properties of the majorite-pyrope garnet were approximated by the Redlich-Kister equation, in

Table 3. Conditions of equilibration experiments on the enstatite-pyrope join and the average compositions of phases

Run #	Mix[a]	t[b] (h)	P_g[c] (bar)	P_s[d] (kbar)	T_s[e] (°C)	Phase[f]	An.[g]	Cations/6 oxygens			Sum	X_{Py}
								Mg	Al	Si		
535	E	7.2	160	100	1450	Ga	22	1.575	0.865	1.564	4.004	0.862
					1650	En	5	2.005	0.017	1.985	4.007	
495	E	7.5	250	125	1650	Ga	36	1.660	0.725	1.626	4.011	0.717
					1450	Ga	11	1.647	0.759	1.607	4.013	0.749
					1650	En	3	2.004	0.008	1.992	4.004	
350	E	7.0	320	140	1650	Ga	29	1.679	0.639	1.683	4.001	0.638
					1450	Ga	32	1.671	0.676	1.657	4.004	0.673
					1650	En	4	2.026	0.005	1.982	4.013	
335	E	6.7	400	152	1650	Ga	35	1.763	0.486	1.754	4.003	0.485
					1450	Ga	27	1.744	0.521	1.738	4.003	0.520
					1650	En	9	1.991	0.005	2.001	3.997	
342	E	7.0	460	157	1650	Ga	25	1.785	0.440	1.777	4.002	0.439
					1450	Ga	19	1.760	0.489	1.753	4.002	0.488
					1650	En	9	1.992	0.004	2.001	3.997	
367	E	6.5	500	160	1650	Ga	35	1.841	0.346	1.820	4.007	0.343
					1450	Ga	14	1.818	0.364	1.818	4.000	0.364
					1650	En	9	2.000	0.005	1.996	4.001	
477	E	7.1	600	165	1450	Ga	27	1.825	0.358	1.818	4.001	0.357
					1450	En	3	2.006	0.001	1.996	4.003	
					1250	Bt	3	2.991	0.002	1.503	4.496	
551	E	7.2	600	165	1550	Ga	11	1.887	0.247	1.871	4.005	0.246
					1550	En	5	1.997	0.002	2.000	3.999	
439	E	5.7	600	165	1650	Ga	63	1.964	0.087	1.953	4.004	0.086
					1650	En	13	2.008	0.001	1.995	4.004	
629	E	1.0	600	165	1650	Ga	7	1.950	0.123	1.933	4.006	0.122
					1650	En	3	2.003	0.005	1.995	4.003	
455	E	6.0	600	165	1750	Ga	54	1.960	0.113	1.935	4.008	0.112
447	E	6.0	600	165	1850	Ga	21	1.932	0.148	1.923	4.003	0.148

[a–g] Explanations in Table 1

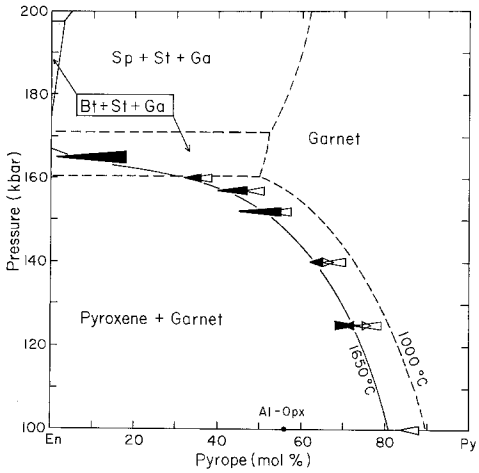

Fig. 5. Pressure-composition phase diagram for the enstatite-pyrope join. The *solid arrows* indicate the range of compositions of the garnet coexisting with enstatite at 1650° C observed in the hot spot, *open arrows* indicate the compositions in the cold end of the samples at 1450° C

which only the excess entropy terms were necessary to express the deviation from complete disorder (J, K):

$$RT\ln a_{Mj} = 2RT\ln X_{Mj} + 7TX_{Py}^2 - 18T(4X_{Py}^3 - 3X_{Py}^2).$$

The resulting mixing parameters indicate that the majorite-pyrope garnet behaves as athermal solution ($G^{xs} = -TS^{xs}$); the consequence of mixing of two cations of very different sizes in one crystallographic site (e.g. Guggenheim 1967).

The $P-T$ phase diagram for the system $MgO-Al_2O_3-SiO_2$ shown in Fig. 6 was calculated using the parameters (J, bar, K) based primarily on the experimental studies of Sawamoto (1987) and Ito and Takahashi (1988), and on the enthalpy measurements reported by Akaogi et al. (1984, 1987):

2OEn = Mj,	$\Delta G = 145950 + 9.4T - 1.14P$,
2CEn = Mj,	$\Delta G = 129350 - 3.0T - 0.74P$,
Mj = 2Bt + 2St,	$\Delta G = -9100 + 12.0T - 0.08P$,
Mj = 2Sp + 2St,	$\Delta G = 4550 + 17.4T - 0.20P$,
Mj = 4 Ilmenite,	$\Delta G = 21330 + 16.14T - 0.274P$,
Mj = 4 Perovskite,	$\Delta G = 141420 + 4.7T - 0.714P$,
OEn = CEn,	$\Delta G = 8300 + 6.2T - 0.20P$,
Fo = Bt,	$\Delta G = 30000 + 7.2T - 0.29P$,
Bt = Sp,	$\Delta G = 6825 + 2.7T - 0.06P$,
Sp = Perovskite + MgO,	$\Delta G = 14950 - 1.93T - 0.05P$.

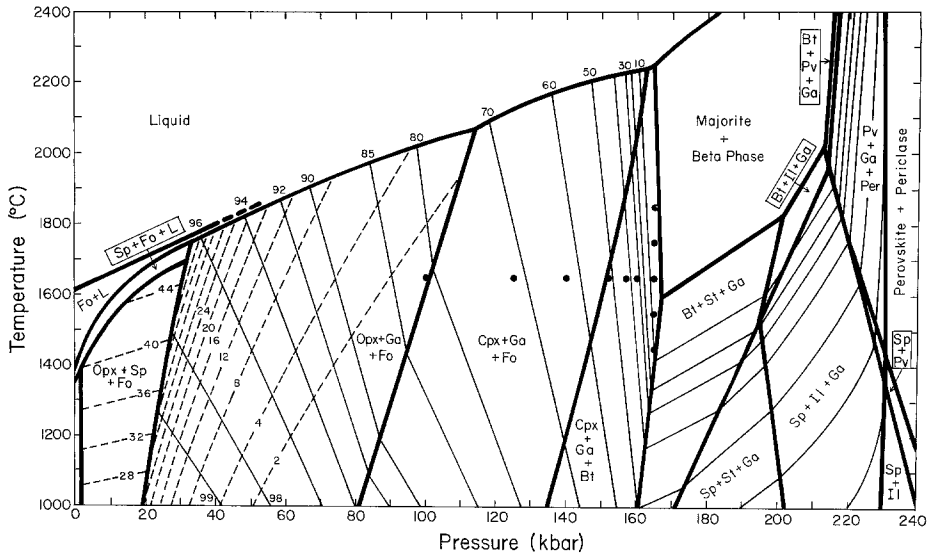

Fig. 6. Pressure-temperature phase diagram for the system $MgO-Al_2O_3-SiO_2$. *Solid dots* show the locations of the experiments from Table 3. *Heavy lines* are univariant boundaries and melting curves. *Thin solid lines* are isopleths indicating the pyrope content of garnet (in mol%); *thin dashed* isopleths indicate the pyrope content of the coexisting pyroxene, based on Gasparik and Newton (1984). Melting estimated from the data of MacGregor (1974) and Presnall and Gasparik (1989). Supersolidus melting relations are incomplete

At equilibrium, $RT \ln K_{eq} = -\Delta G$. Clinoenstatite was considered here as a unique high-pressure polymorph, a close analogue of $Mg_2Ge_2O_6$ clinopyroxene (Ross and Navrotsky 1988). Thus, ΔV for the orthoenstatite-clinoenstatite transition (Pacalo and Gasparik 1989) was set at -2 cm^3/mol of $Mg_2Si_2O_6$ (compared with -2.34 cm^3/mol of $Mg_2Ge_2O_6$). The $MgSiO_3$ ilmenite and perovskite were assumed to be ideal.

In two 6 h experiments at 165 kbar, 1650° and 1750° C (runs 439, 455), majorite-rich garnet with the composition close to enstatite nucleated in the matrix of the samples. However, in a 1 h experiment at 165 kbar, 1650° C (run 629), the experimental product was mostly enstatite; the majorite-rich garnet was observed only on the original pyrope and aluminous pyroxene seeds. Apparently, run durations in excess of 1 h were needed to nucleate the majorite-rich garnet in the matrix due to release of aluminum from slowly dissolving seeds. Some garnets in the 6 h experiments had pyrope contents as low as 1 mol%, and differed only slightly in composition from the coexisting enstatite. However, it was easy to distinguish the two phases under electron beam because enstatite exhibited fluorescence while garnet did not. The large amount of the newly-formed garnet and its low aluminum content reflect the close vicinity of the enstatite-majorite boundary, which was observed in the pure $MgO-SiO_2$ system at 165 kbar, 2150° C (Presnall and Gasparik 1989). In this 1 h long experiment at 2200° C nominal temperature, the boundary located in the cold end of the sample was very sharp, and had majorite at higher temperatures. This demonstrated the negative slope of the enstatite-majorite transition, in contrast to the positive slope reported by Kato and Kumazawa (1985) and Sawamoto (1987). The same experiment also produced eutectic melting (for the bulk composition $En_{80}Fo_{20}$, wt%) in the hot spot (2250° C), with the eutectic melt composition close to $En_{50}Fo_{50}$ (wt%).

At 165 kbar, 1850° C (run 447), garnet did not nucleate in the matrix; there was evidence that melt escaped from the molybdenum capsule early in the experiment resulting in very limited equilibration and dissolution of pyrope seeds. At lower temperatures, 1450° and 1550° C, the lack of the newly-formed garnet was apparently the consequence of the increased distance from the stability field of majorite, which does not extend below 1600° C. A sharp phase boundary between enstatite and beta phase + stishovite, with enstatite at higher temperatures, was present in the center of the sample at 165 kbar, 1400° C (run 477).

At 165 kbar, corundum inclusions in the pyrope seeds transformed into a highly birefringent phase (blue or green under crossed polars) surrounded by pure pyrope. Microprobe analyses indicated that this phase had pure Al_2O_3 composition. It is possible that the new Al_2O_3 polymorph is an analogue of Rh_2O_3 II reported by Shannon and Prewitt (1970).

2 Enstatite – diopside – grossular – pyrope

The first data on the solubility of pyroxene in the garnet coexisting with two pyroxenes in the CMAS system were reported by Yamada and Takahashi (1984) at 50–100 kbar, and by Ito and Takahashi (1987) at higher pressures.

In this study, experiments were conducted at 100–165 kbar and 1250–1750° C (Table 1). The starting materials (Table 2) contained large seeds of synthetic orthoenstatite, diopside, pyrope and grossular. Microprobe analyses were obtained at 15 kV accelerating potential and 25 nA beam current using natural enstatite and grossular for standards. The compositional fields obtained from the pyrope and grossular seeds overlap in most experiments indicating that equilibrium was attained.

The lead flux used in the initial experiments did not enter the garnet nor the enstatitic pyroxene; however, up to 10 at% of Pb was present in the M2 site of the diopsidic pyroxene. As a consequence of the decreased activity of calcium in the pyroxene, it is expected that the calcium content of the coexisting garnet was also lowered, but most likely without any effect on the pyroxene content of garnet. Due to the problem with lead in the diopsidic pyroxene, V_2O_5 was tested as a flux; vanadium did not enter the pyroxene, but small amounts were detected in the garnet. Vanadium substituted for aluminum in the octahedral site of garnet as V^{3+}, and had a significant effect on the pyroxene solubility in garnet. The calcium content of garnet was presumably not affected by the presence of vanadium. Thus, neither of the two fluxes used was perfectly suitable for the study of the CMAS system. However, the lead flux

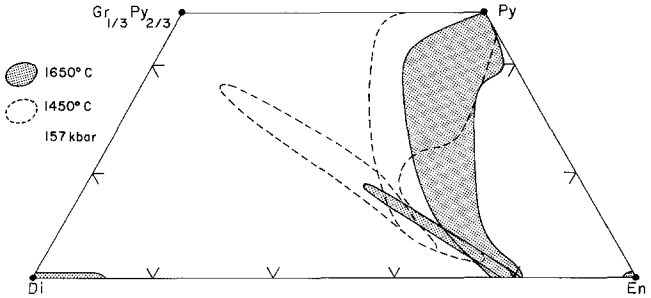

Fig. 7. Compositions of garnet and the coexisting two pyroxenes in the CMAS system at 157 kbar (run 182). *Solid envelopes* enclose the compositions from the hot spot; *dashed envelopes* indicate the compositions from the cold end of the sample

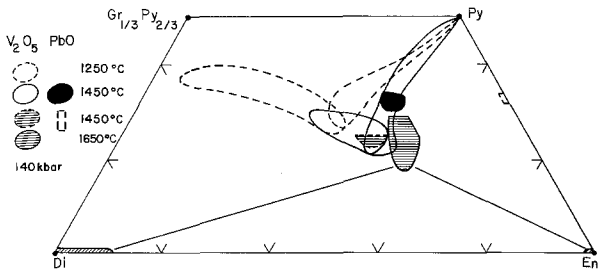

Fig. 9. Compositions of garnet coexisting with two pyroxenes in the CMAS system at 140 kbar. *Solid envelopes* enclose the compositions from the hot spot, *dashed envelopes* indicate the compositions from the cold end of the samples. The V_2O_3 contents of garnet were omitted

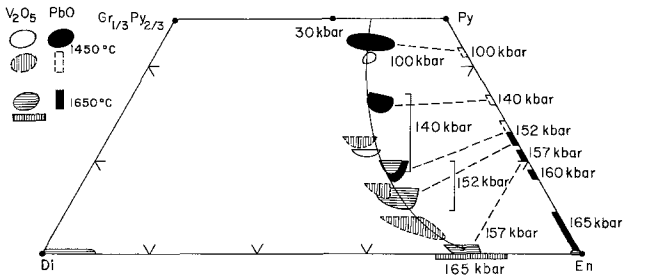

Fig. 8. Compositions of garnet coexisting with two pyroxenes in the CMAS system, or with enstatite in the MAS system, at 100–165 kbar and 1450–1650° C. *Solid envelopes* enclose the compositions from the hot spot, *dashed envelopes* indicate the compositions from the cold end of the samples. The *solid curve* with an *arrow* indicates the compositional trend followed by the garnet with increasing pressure. The *dashed lines* show the effect of calcium on the pyroxene content of garnet. The data point at 30 kbar (1500° C) is from Howells and O'Hara (1978). The V_2O_3 contents of garnet were omitted

seemed appropriate for determining the pyroxene content of garnet, and the vanadium flux appeared suitable for determining the calcium content.

At 157 kbar, 1650° C (run 182), garnet with the composition $En_{79}Di_{21}$ formed on the enstatite-diopside join (Fig. 7). While in this experiment the pyroxene-rich garnet compositions were limited to the original pyrope and grossular seeds, at 165 kbar and the same temperature, a new enstatite-diopside garnet nucleated in the matrix of the sample. Although, the range of the garnet compositions on the enstatite-diopside join was wider at 165 kbar than at 157 kbar (see Fig. 8), both pyroxenes were still present. Apparently, a two-pyroxene assemblage formed metastably from the starting material at the beginning of the experiment at 165 kbar, and did not transform completely to garnet even after 7 h.

Figure 8 summarizes all data obtained in the CMAS system. Only the overlapping or the most pyroxene-rich portions of the compositional fields are shown. The compositional trend indicated by the solid line with an arrow satisfies quite well all data in the temperature range 1450°–1650° C.

Figure 9 illustrates the effect of temperature on the calcium content and the effect of vanadium on the pyroxene content of garnet at 140 kbar. In the experiments with the vanadium flux, the most equilibrated portions of the compositional fields from the cold end of the sample at 1650° C and from the hot spot of the sample at 1450° C overlap, indicating a 200° C temperature difference between the hot spot and the cold end of the samples. Thus, the data from the cold end of the sample at 1450° C give the garnet compositions at 1250° C. The results indicate, that the pyroxene content of the garnet increases with increasing temperature while the calcium content decreases, which is consistent with the observations of Yamada and Takahashi (1984).

The compositions of the two pyroxenes coexisting with garnet in the CMAS system are independent of the garnet composition, because the aluminum content of the pyroxenes is negligible at these high pressures. The enstatite-diopside join at 100 kbar was discussed previously in the context of the temperature calibration. At higher pressures and temperatures of 1450–1650° C, the solubilities are quite limited and correspond typically to 5–15 mol% of enstatite in the diopsidic pyroxene and 1–3% of diopside in the enstatitic pyroxene. This is in contrast to the extensive solubilities, undoubtedly metastable, reported by Liu (1987) in his work with the diamond cell.

3 Enstatite – jadeite – pyrope

Until recently, experimental investigation of the enstatite-jadeite join has been limited despite its importance for the petrogenesis of basalts. At the conditions of the earth's crust, the enstatite-jadeite join is metastable; the stable join is albite-forsterite which produces the thermal divide responsible for the separation of olivine tholeiites and alkali basalts (Yoder and Tilley 1962). At pressures of 20–30 kbar, clinopyroxene forms from albite + forsterite, and the enstatite-jadeite join becomes the new thermal divide (Windom and Unger 1988). At higher pressures, two coexisting pyroxenes form the stable assemblage.

The compositions of coexisting clinopyroxene and orthopyroxene on the enstatite-jadeite join, obtained with a DIA-type multianvil apparatus (SAM-85, described by Gwanmesia 1987), were first reported by Gasparik (1986). At 60 kbar, 1400° C, clinopyroxene with the composition $En_{60}Jd_{40}$ was found to coexist with the $En_{88}Jd_{12}$ orthopyroxene (Table 4, Fig. 10). This result confirmed the extensive solubilities of enstatite in jadeitic clinopyroxene that were indicated earlier by the synthesis experiments of Yoder and Tilley (1962) and Kushiro (1965). Shortly after, Pierson and Windom (1986) reported their experimental study of the enstatite-jadeite solvus at 25 kbar and 900°–1300° C. Additional data obtained with SAM-85 at 60 kbar and

Table 4. Conditions of equilibration experiments in the NMAS system and the average compositions of phases

Run #	Mix[a]	t[b] (h)	P_g[c] (bar)	P_s[d] (kbar)	T_s[e] (°C)	Phase[f]	An.[g]	Cations/6 oxygens				Sum
								Na	Mg	Al	Si	
8	F	8.0		60	1200	Jd	10	0.543	0.885	0.570	1.995	3.992
					1200	En	25	0.118	1.760	0.134	1.990	4.002
7	F	7.0		60	1300	Jd	28	0.433	1.094	0.454	2.004	3.985
					1300	En	34	0.123	1.738	0.135	1.999	3.995
5	G	5.0		60	1400	Jd	23	0.407	1.192	0.425	1.983	4.007
					1400	En	23	0.126	1.764	0.146	1.977	4.013
58	F	7.0	160	100	1450	Ga	3	0.390	1.088	0.612	1.900	3.990
					1450	Jd	7	0.421	1.168	0.395	2.015	3.999
					1450	En	15	0.214	1.603	0.182	2.009	4.008
82	G	7.0	160	100	1550	Ga	2	0.492	0.908	0.645	1.939	3.984
					1550	Jd	11	0.429	1.141	0.424	2.005	3.999
					1550	En	8	0.240	1.513	0.241	2.002	3.996
78	G	7.2	180	107	1550	Ga	10	0.470	0.967	0.641	1.918	3.996
					1550	Jd	17	0.470	1.073	0.458	2.002	4.003
					1550	En	4	0.227	1.516	0.285	1.972	4.000
84	G	7.0	180	107	1650	Ga	11	0.449	1.048	0.574	1.933	4.004
					1650	Jd	25	0.470	1.089	0.452	1.999	4.010
					1650	En	3	0.164	1.668	0.157	2.007	3.996
72	G	7.1	200	113	1550	Ga	3	0.417	1.087	0.612	1.893	4.009
					1550	Jd	12	0.501	0.994	0.500	2.003	3.998
					1550	En	5	0.129	1.686	0.193	1.980	3.988
67	F	7.0	230	121	1550	Ga	10	0.473	0.987	0.609	1.932	4.001
					1550	Jd	17	0.483	1.047	0.465	2.007	4.002
					1550	En	1	0.096	1.839	0.113	1.972	4.020
501	F	8.0	294	135	1650	Ga	4	0.519	0.983	0.520	1.989	4.011
					1650	Jd	8	0.614	0.903	0.395	2.099	4.011
					1650	En	4	0.059	1.926	0.036	1.995	4.016
53	F	5.0	320	140	1350	Ga	21	0.364	1.240	0.436	1.962	4.002
					1350	En	4	0.045	1.901	0.063	1.991	4.000
54	F	6.0	320	140	1500	Ga	1	0.471	1.045	0.496	1.988	4.000
					1500	Jd	5	0.641	0.728	0.616	2.014	3.999
					1500	En	5	0.066	1.863	0.099	1.977	4.005
61	F	6.0	320	140	1650	Ga	5	0.373	1.210	0.410	1.994	3.987
88	H	7.0	320	140	1650	Ga	6	0.472	1.082	0.448	2.005	4.007
95	I	6.2	320	140	1650	Ga	4	0.395	1.243	0.389	1.988	4.015
					1650	En	15	0.030	1.964	0.025	1.992	4.011
163	J	5.0	320	140	1650	Ga	1	0.472	1.126	0.431	1.995	4.024
					1650	Jd	15	0.708	0.629	0.632	2.034	4.003
80	F	7.0	400	152	1650	Ga	43	0.359	1.277	0.361	2.001	3.998
					1650	En	6	0.021	1.982	0.018	1.990	4.011
380	K	7.0	400	152	1650	Ga	7	0.416	1.235	0.291	2.060	4.002
					1650	En	2	0.018	1.978	0.016	1.994	4.006
					1650	Fo	3	0.021	2.969	0.012	1.501	4.503
					1450	N[h]	1	3.127	1.405	0.139	1.411	6.082
387	L	7.0	400	152	1850	Ga	3	0.219	1.515	0.279	1.978	3.991
					1850	En	5	0.019	1.972	0.018	1.996	4.005
					1850	Fo	3	0.012	2.963	0.013	1.506	4.494
					1650	Px	6	0.842	0.732	0.025	2.405	4.004
389	K	7.0	500	160	1650	Ga	23	0.254	1.503	0.254	1.995	4.006
					1450	Ga	3	0.274	1.471	0.266	1.996	4.007
					1650	En	2	0.049	1.946	0.016	2.003	4.014
					1650	Bt	2	0.036	2.959	0.018	1.498	4.511
					1450	N[h]	1	2.811	1.463	0.039	1.537	5.850
520	M	7.3	600	165	1650	Ga	10	0.141	1.378	0.863	1.628	4.010
					1650	Jd	3	0.958	0.113	0.954	1.988	4.013
								Pb	Mg	Al	Si/10 ox.	
					1450	P[i]	7	1.067	0.004	2.012	2.955	6.038

[a–g] Explanations in Table 1; [h] Na_2MgSiO_4; [i] $PbAl_2Si_3O_{10}$, a phase of purple color

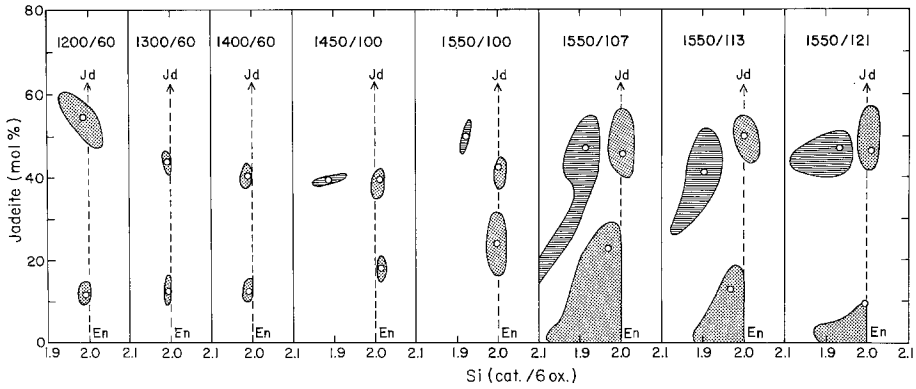

Fig. 10. Compositions of coexisting pyroxenes (*dotted pattern*) and garnet (*ruled pattern*) in the NMAS system. *Envelopes* enclose the observed compositions, *open circles* indicate the averages listed in Table 4

1200°–1300° C (Gasparik 1987) are summarized in Table 4 and Fig. 10.

In this study, new data were obtained in the pressure range of 100–160 kbar using the same techniques that were successfully applied at lower pressures. The starting materials (Table 2) contained sodium disilicate flux and large seed crystals of synthetic jadeite, orthoenstatite and orthopyroxene with the composition $En_{44}Py_{56}$. Microprobe analyses were obtained at 5 kV accelerating potential and 30 nA beam current using natural enstatite and albite for standards.

In most experiments, sodium-rich garnet formed from the aluminous orthopyroxene seeds. Similar sodium-rich garnets were first synthesized by Ringwood and Major (1971) at 180 kbar, 1000° C; however, their garnets contained calcium instead of magnesium. Garnet analyses were identified by an excess of aluminum with respect to sodium and the corresponding deficiency in silicon. The presence of garnet was also confirmed optically in thin sections.

The experiments at 100 kbar (Fig. 10) contained only traces of garnet; a wide range of garnet compositions was found at 107 kbar. Figure 11 shows the range of compositions obtained by electron microprobe from an experiment at 107 kbar, 1650° C (run 84). The garnet compositions plot close to the join $Py-En_{50}Jd_{50}$, but do not quite reach the pyroxene join. The analyses form two clusters which could be interpreted as coexistence of two garnet phases. At higher pressures, the sodium-rich garnet formed a complete solid solution with pyrope.

Figures 10 and 11 show a substantial amount of tetrahedral aluminum in the enstatitic pyroxene at 107 kbar and higher pressures. None of the sodium-free systems investigated showed any significant tetrahedral aluminum in the pyroxene phases, nor was it present in the NMAS system at 100 kbar. The amount of tetrahedral aluminum is substantially lower at 135–160 kbar (Fig. 12 and 13). The maximum contents of tetrahedral aluminum seem to coincide with the orthopyroxene-clinopyroxene transition in the enstatitic pyroxene. Thus, it is tentatively proposed that the enstatitic clinopyroxene is capable of incorporating the observed high contents of the Mg-Tschermak component ($MgAl_2SiO_6$). However, it is also possible that these compositions represent metastable or quench products.

Figure 12 shows the results of several experiments at the P–T conditions at which garnet first formed from two pyroxenes on the enstatite-jadeite join. Along this univariant boundary, the jadeite content of the garnet increases with increasing temperature from approximately 40 mol% at 1350° C, to 47% at 1500° C, and 52% at 1650° C. At

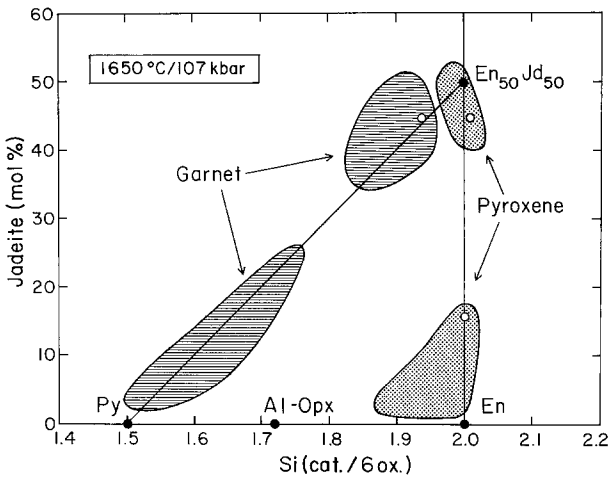

Fig. 11. Compositions of coexisting pyroxenes (*dotted pattern*) and garnet (*ruled pattern*) in the NMAS system at 107 kbar, 1650° C. *Envelopes* enclose the observed compositions, *open circles* indicate the averages listed in Table 4

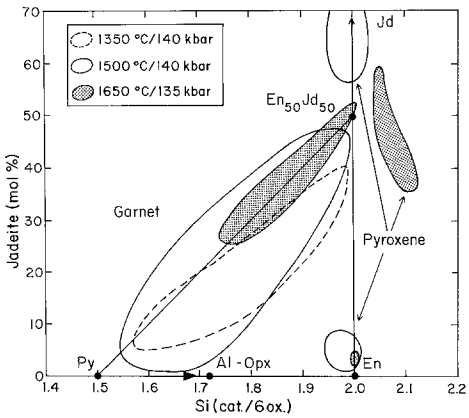

Fig. 12. Compositions of coexisting pyroxenes and garnet in the NMAS system at 135–140 kbar and 1350–1650° C

140 kbar, 1500° C (run 54), the compositions of both coexisting pyroxenes were obtained in addition to garnet. At the same pressure and 1650° C, the stability field of garnet on the enstatite-jadeite join was much wider; several experiments with different bulk compositions were needed to determine its width and the compositions of both pyroxenes (Table 4). Thus, the univariant boundary indicating the formation of garnet from two pyroxenes on the enstatite-jadeite join has a negative slope.

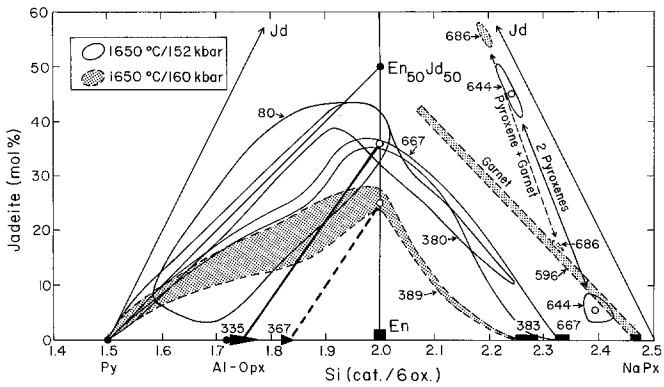

Fig. 13. Compositions of coexisting pyroxenes and garnet in the NMAS system at 152 and 160 kbar, 1650° C. The *heavy solid* and *dashed lines* indicate the equilibrium solubilities of pyroxene in the garnet coexisting with the enstatitic pyroxene. *Envelopes* enclose the observed compositions, *open circles* indicate averages. Experiments are labeled by the run numbers listed in Tables 4 and 5

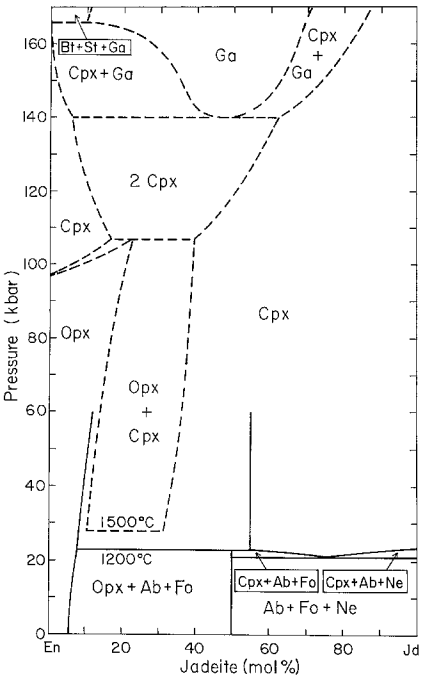

Fig. 14. Pressure-composition phase diagram for the enstatite-jadeite join at 1200° C (*solid lines*) and 1500° C (*dashed lines*)

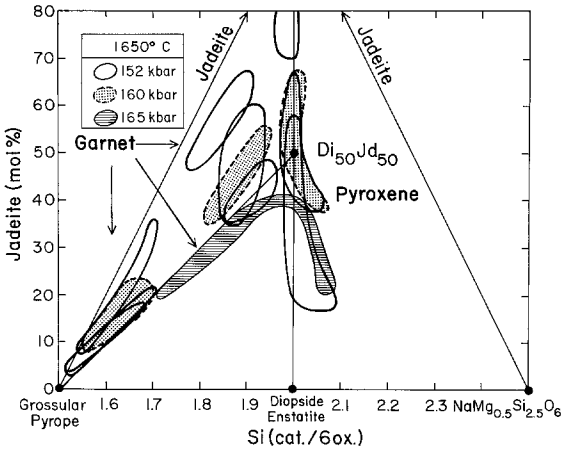

Fig. 15. Compositions of coexisting pyroxene and garnet in the NCMAS system (near the diopside-jadeite join) at 152–165 kbar, 1650° C

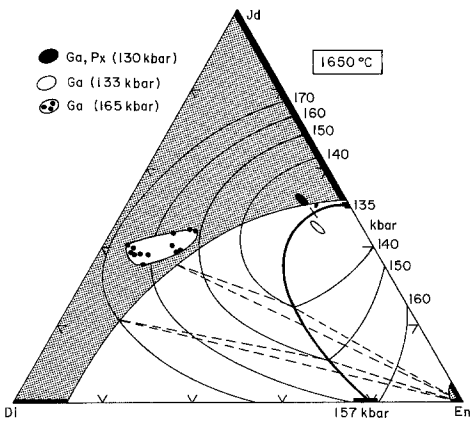

Fig. 16. Phase relations in the enstatite-diopside-jadeite system at 1650° C. The expansion of the garnet stability field with pressure is indicated by isobars (*solid thin lines*). The *heavy line* is the locus of the compositions of garnet in equilibrium with two pyroxenes, the *dashed tie lines* connect hypothetical compositions of the three coexisting phases at 140 and 150 kbar. The *solid bars* show the experimentally determined range of solid solutions at 135 kbar on the En–Jd join, and at 157 kbar on the En–Di join. The *shaded areas* indicate the maximum extent of the ternary solutions of the two pyroxenes in equilibrium with the garnet. The *solid dots* for the experiment at 165 kbar represent the actual microprobe analyses

The stability field of garnet on the enstatite-jadeite join expands with increasing pressure or temperature toward enstatite, and also beyond the enstatite-jadeite join in the direction of the enstatite-NaPx join. This expansion of the garnet stability was determined at 152 and 160 kbar, 1650° C (Fig. 13). At 160 kbar, a new phase with the composition close to Na_2MgSiO_4 was observed instead of the melt in the cold end of the sample.

On the basis of these new high-pressure experiments in the NMAS system, a tentative pressure-composition phase diagram for the enstatite-jadeite join is presented in Fig. 14.

4 Diopside – jadeite

The diopside-jadeite join was experimentally investigated at 152–165 kbar, 1650° C (Table 5, Fig. 15) to determine if garnet would stabilize on the join as observed in other systems. Several bulk compositions were used to cover a large portion of the join; starting materials (Table 2) contained sodium disilicate flux, and a small excess of CaO over MgO was used to maximize the Ca/(Ca+Mg) ratio of the crystalline phases. The starting materials were seeded with large crystals of diopside, jadeite, Ca-Tschermak pyroxene ($CaAl_2SiO_6$) and orthopyroxene with the composition $En_{44}Py_{56}$. Microprobe analyses were obtained at 15 kV accelerating potential and 15 nA beam current using natural enstatite, grossular and albite for standards. All garnet analyses were obtained from the Ca-Tschermak seeds which were identified by seed remnants converted to grossular and corundum. The sodium-rich garnet compositions were limited to the perimeter of these centers of inho-

mogeneity. The rest of the samples was pyroxene, as confirmed by optical observations in thin sections.

Only traces of garnet were found at 152 and 160 kbar. The garnet analyses always plot in two clusters located almost completely within the compositional triangle (Gr, Py) – $Di_{50}Jd_{50}$ – Jd (Fig. 15). The solubility of diopside in garnet beyond the (Gr, Py) – $Di_{50}Jd_{50}$ join was minimal. This limitation in the diopside solubility was convincingly demonstrated in an experiment with the lowest sodium bulk content (run 264). Most of the pyroxene in the experimental charge had 30–40 mol% of jadeite determined by the bulk composition of the sample. However, the composition of the garnet approached $Di_{50}Jd_{50}$ from the Gr – Py join even though the original Ca-Tschermak seeds did not contain sodium. Moreover, the pyroxene immediately adjacent to the garnet had also elevated sodium contents, typically in the range of 45–55% jadeite. Apparently, the pyroxene was approaching a composition in equilibrium with the garnet.

At 165 kbar (run 515), the amount of garnet in the sample increased substantially, and the most equilibrated compositions approached closely the diopside-jadeite join (Fig. 16). A short extrapolation of the trend indicated by the data to the diopside-jadeite join predicts the formation of the first garnet on the join with the composition $Di_{63}Jd_{37}$ around 170 kbar.

5 Enstatite – NaPx

Gasparik (1988) reported the synthesis of a new pyroxene phase $NaMg_{0.5}Si_{2.5}O_6$ (NaPx). The potential stability of this pyroxene was indicated by the microprobe analyses of pyroxenes from the study of the enstatite-jadeite and diopside-jadeite joins, which often showed an excess of silicon over 2 for 6 oxygens. Phase equilibrium data were obtained at 80–165 kbar and 1450–1750° C on the stability of NaPx, its transformation to garnet, and on the solubility of enstatite, diopside and jadeite in NaPx and its garnet polymorph (Table 5).

NaPx is highly ordered with P2/n structure (Angel et al. 1988). It melts incongruently at 80 kbar, 1450° C to enstatite, coesite and liquid (run 657) and, as $K_2Si_4O_9$ with the wadeite structure (Swanson and Prewitt 1983), could be stable to much lower pressures despite the presence of octahedral silicon. NaPx transforms to garnet at 154 kbar, 1650° C (Fig. 17). At these conditions, the pure NaPx bulk composition produces pyroxene or garnet with 3 mol% enstatite, stishovite and sodium-rich melt. At 155–160 kbar, fine-grained pyroxene was present in the cold end of the samples, in addition to a much coarser garnet in the rest of the samples. This indicates that the pyroxene-garnet transition has a negative slope. At the transition, the compositions of the coexisting pyroxene and garnet were identical.

On the enstatite-NaPx join (Fig. 17), two coexisting pyroxenes were produced at 80–154 kbar; however, from the starting material seeded with pyrope, garnet with the composition $En_{33}NaPx_{67}$ formed at 152 kbar (run 667). The solubility of the NaPx component in enstatite is minor, but the enstatite solubility in the coexisting NaPx-rich pyroxene is substantially higher and increases with pressure from En_{20} at 80 kbar to En_{29} at 152 kbar. The enstatite solubility in the NaPx-rich pyroxene coexisting with enstatite is temperature independent: the compositional variations within the 200° C temperature difference between the

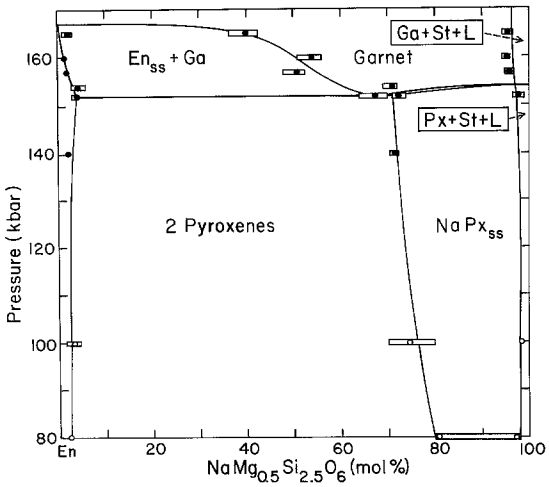

Fig. 17. Pressure-composition phase diagram for the enstatite-NaPx join at 1450° C (*open circles*) to 1650° C (*solid dots*). The *rectangles* show the range of the observed compositions, the *solid dots* and *open circles* indicate the averages listed in Table 5

hot spot and the cold end of the samples were minimal. Above 152 kbar, the solubility of the enstatite component in garnet increases with pressure to En_{60} at 165 kbar, and is projected to be complete at 167 kbar.

In the En – Jd – NaPx system, the first garnet forms near the $En_{48}Jd_{52}$ composition at 135 kbar, 1650° C (run 501), and with increasing pressure the wedge-shaped stability field of garnet expands reaching the $En_{33}NaPx_{67}$ composition at 152 kbar. Near the Jd – NaPx join at 152 kbar, 1650° C (run 644), NaPx-rich pyroxene with the composition $En_{15}Jd_6NaPx_{79}$ coexists with Jd-rich pyroxene with the composition $En_7Jd_{45}NaPx_{48}$ (Fig. 13). Thus, the garnet forming from NaPx at 154 kbar is also the first garnet on the jadeite-NaPx join. At higher pressures, the jadeite contents of the coexisting pyroxene and garnet on the jadeite-NaPx join increase with increasing pressure (run 686). The En – Jd – NaPx system can have 3 coexisting pyroxenes below 135 kbar.

6 Enstatite – diopside – jadeite

The first garnet in the En – Di – Jd system forms at lower pressures than the first appearance of garnet on the constituent En – Di and En – Jd binary joins: a ternary garnet would not be stable unless its formation expands the stability field of garnet. The composition of this first garnet at 1650° C was estimated from two experiments at 130 and 133 kbar (Table 5, Fig. 16). At 130 kbar (run 406), the most pyroxene-rich garnet contained 7 mol% of pyrope; thus, a short extrapolation from the pyrope apex was necessary to project its composition to the En – Di – Jd system. At 133 kbar (run 544), the most equilibrated garnet had a small amount of the NaPx component. Based on these results, the formation of the first garnet with the composition $En_{42}Di_9Jd_{49}$ is predicted to be at 133 kbar for 1650° C temperature.

The tentative phase relations for the En – Di – Jd system at 1650° C are shown in Fig. 16. The first garnet in the ternary system forms from two pyroxenes at 133 kbar; with increasing pressure the stability field of garnet expands in all directions. However, the composition of the garnet coex-

Table 5. Conditions of equilibration experiments in the NCMAS system and the average compositions of phases

Run #	Mix[a]	t[b] (h)	P_g[c] (bar)	P_s[d] (kbar)	T_s[e] (°C)	Phase[f]	An.[g]	Cations/6 oxygens					Sum
								Na	Ca	Mg	Al	Si	
Di–Jd join													
235	N	7.0	400	152	1650	Ga	2	0.618	0.333	0.318	0.839	1.891	3.999
					1650	Px	10	0.711	0.280	0.313	0.712	1.992	4.008
264	O	7.0	400	152	1650	Ga	3	0.429	0.634	0.476	0.552	1.924	4.015
					1650	Px	5	0.505	0.514	0.519	0.482	1.995	4.015
279	P	7.0	400	152	1650	Ga	3	0.432	0.617	0.415	0.614	1.915	3.993
					1650	Px	27	0.536	0.478	0.483	0.505	2.006	4.008
290	P	7.0	500	160	1650	Ga	4	0.513	0.545	0.396	0.641	1.920	4.015
					1650	Px	22	0.571	0.428	0.469	0.530	2.011	4.009
					1650	Pv	6	0.013	1.977	0.004	0.034	1.981	4.009
515	O	6.6	600	165	1650	Ga	5	0.441	0.540	0.638	0.375	2.020	4.014
					1650	Di	5	0.389	0.549	0.706	0.355	2.009	4.008
					1650	Jd	4	0.468	0.502	0.610	0.424	2.009	4.013
					1650	Pv	1	0.060	1.944	0.025	0.039	1.971	4.039
En–NaPx join													
657	Q	8.0	116	80	1450	G[h]	4	1.221	0	0.472	0.002	2.457	4.152
					1450	Cs	5	0	0	0	0.001	2.999	3.000
					1400	En	4	0.023	0	1.988	0	2.000	4.011
					1400	Px	4	0.831	0	0.780	0	2.402	4.013
					1250	Px	6	0.997	0	0.532	0	2.484	4.013
306	R	7.0	160	100	1450	Px	7	0.744	0.043	0.838	0.002	2.372	3.999
					1450	En	3	0.044	0.009	1.937	0.005	2.012	4.007
322	Q	7.0	160	100	1450	Px	10	0.988	0	0.524	0	2.491	4.003
651	R	7.0	320	140	1650	Px	10	0.718	0.030	0.908	0.001	2.350	4.007
					1450	Px	12	0.736	0.050	0.870	0.001	2.355	4.012
					1650	En	8	0.020	0.003	1.985	0	2.001	4.009
299	R	6.9	400	152	1650	Px	9	0.745	0.055	0.838	0.019	2.353	4.010
					1450	Px	7	0.772	0.049	0.809	0.007	2.373	4.010
					1650	En	3	0.085	0.005	1.880	0.001	2.035	4.006
315[i]	Q	6.0	400	152	1650	Px	14	0.983	0	0.536	0	2.486	4.005
667	S	7.0	400	152	1650	Ga	43	0.666	0.025	0.971	0.005	2.332	3.999
					1450	Ga	12	0.662	0.027	0.983	0.012	2.321	4.005
					1650	Px	6	0.726	0.024	0.893	0.006	2.355	4.004
					1450	Px	11	0.719	0.024	0.903	0.005	2.353	4.004
					1650	En	2	0.057	0.006	1.932	0.001	2.016	4.012
636	R	7.0	420	154	1650	Px	15	0.717	0.051	0.880	0.002	2.354	4.004
					1650	En	3	0.033	0.005	1.929	0.002	2.023	3.992
611	T	6.6	430	155	1650	Ga	15	0.919	0	0.629	0.004	2.452	4.004
					1450	Ga	12	0.894	0	0.657	0.006	2.443	4.000
					1450	Px	11	0.786	0	0.815	0	2.396	3.997
404	R	7.0	460	157	1650	Ga	25	0.512	0.018	1.235	0.002	2.244	4.011
					1650	En	2	0.018	0.006	1.994	0.001	1.995	4.014
604	U	6.3	460	157	1650	Ga	13	0.955	0	0.563	0.001	2.479	3.998
					1450	Ga	7	0.935	0	0.582	0.007	2.470	3.994
					1450	Px	1	0.940	0	0.578	0.017	2.463	3.998
383	R	7.0	500	160	1650	Ga	25	0.528	0.023	1.187	0.001	2.262	4.001
					1450	Ga	10	0.564	0.025	1.136	0.002	2.277	4.004
					1650	En	6	0.020	0.008	1.971	0	2.005	4.004
596	U	6.1	500	160	1650	Ga	13	0.952	0	0.570	0	2.477	3.999
					1450	Ga	6	0.958	0	0.561	0.003	2.478	4.000
					1450	Px	3	0.927	0	0.598	0.005	2.466	3.996
507	R	6.3	600	165	1650	Ga	10	0.397	0.019	1.385	0.001	2.198	4.000
					1450	Ga	12	0.401	0.018	1.391	0.002	2.193	4.005
					1650	En	11	0.024	0.004	1.961	0.001	2.011	4.001
586	U	5.8	600	165	1650	Ga	10	0.959	0	0.567	0.001	2.476	4.003

Table 5 (continued)

Run #	Mix[a]	t[b] (h)	P_g[c] (bar)	P_s[d] (kbar)	T_s[e] (°C)	Phase[f]	An.[g]	Cations/6 oxygens					Sum
								Na	Ca	Mg	Al	Si	
En–Di–NaPx system													
256	V	7.1	160	100	1750	Px	18	0.120	0.379	1.460	0.003	2.048	4.010
					1550	Px	4	0.285	0.375	1.207	0.005	2.134	4.006
					1750	En	6	0.019	0.052	1.925	0.001	2.006	4.003
En–Jd–NaPx system													
644	W	7.0	400	152	1650	Px	5	0.854	0	0.701	0.056	2.394	4.005
					1450	Px	4	0.862	0	0.671	0.048	2.413	3.994
					1650	Jd	27	0.935	0	0.374	0.450	2.242	4.001
					1450	Jd	9	0.933	0	0.284	0.640	2.145	4.002
686	W	6.5	500	160	1650	Ga	10	0.811	0	0.679	0.169	2.331	3.990
					1650	Jd	15	0.946	0	0.308	0.554	2.194	4.002
En–Di–Jd system													
406	X	6.5	270	130	1650	Ga	2	0.464	0.129	0.899	0.556	1.953	4.001
					1650	Px	8	0.561	0.151	0.778	0.502	2.018	4.010
					1650	En	6	0.028	0.010	1.954	0.015	2.000	4.007
544	X	7.1	284	133	1650	Ga	3	0.506	0.152	0.898	0.416	2.037	4.009
					1650	Px	50	0.468	0.150	1.020	0.292	2.079	4.009
					1650	En	16	0.028	0.007	1.955	0.019	1.998	4.007

[a–d] Explanations in Table 1
[e] Sample temperature in the hot spot (nominal $T+50°$ C), the center of the sample (nominal T) and the cold end (nominal $T-150°$ C)
[f] In addition to the listed phases, assemblages include stishovite, except where forsterite or beta phase is present
[g] The total number of analyses accepted from the given experiment for each phase
[h] Glass
[i] A single crystal from this experiment was used for the structure determination of NaPx by Angel et al. (1988)

isting with two pyroxenes is limited to the heavy curve in Fig. 16 connecting the first appearances of garnet in the ternary and in the constituent En–Jd and En–Di binary systems. Around 157 kbar, garnet stabilizes on the En–Di join and precludes further coexistence of the two pyroxenes. Enstatite transforms to majorite at 167 kbar. Around 170 kbar, garnet forms on the Di–Jd join, separating the continuous pyroxene solution into two fields. At pressures between 165 kbar and 190 kbar (Tamai and Yagi 1987; Irifune et al. 1989), diopside breaks down to $CaSiO_3$ perovskite and En–Di garnet. At higher pressures, the only stable pyroxene is limited to the jadeite-rich apex of the ternary system.

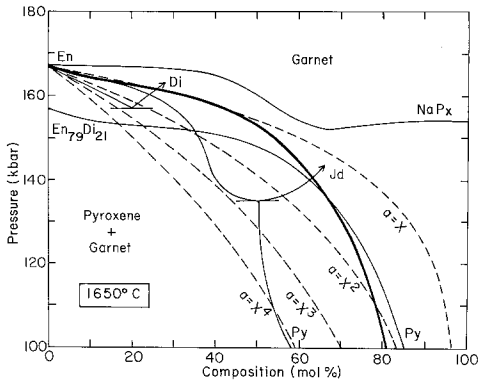

Fig. 18. Pressure-composition phase diagram showing the experimentally determined pyroxene-garnet solvi (*solid curves*) and the calculated solvi (*dashed curves*) for ideal garnets with variable types of disorder

Discussion

The experimentally determined pyroxene-garnet solvi could provide information about order-disorder in the majorite garnets, providing the observed nonideality is primarily caused by ordering. Figure 18 shows several pyroxene-garnet solvi determined in this study, as well as the calculated solvi for ideal garnets with variable types of disorder which define the activities of their components: for a completely ordered garnet, the activity of a component in solution is equal to its mole fraction ($a=X$); for a garnet with the cations completely disordered on the two octahedral sites, applicable to the En–Py join, $a=X^2$; for a garnet with complete disorder on the three cubic sites, applicable to the En–Di join, $a=X^3$; and finally for a garnet with complete disorder on all cubic and octahedral sites, applicable to the En–Jd join, $a=X^4$.

The experimentally determined pyroxene-garnet solvus on the En–Py join is consistent with a completely ordered garnet in the compositional range 1–45 mol% pyrope, but approaches solubilities predicted by complete disorder in the pyrope-rich compositions. This agrees with the observations of disorder in intermediate En–Py garnets based on vibrational spectra (McMillan et al. 1988).

The stable segments of the En–Di and En–Jd solvi indicate solubilities that are intermediate between complete

order and disorder. However, addition of even a small amount of the pyrope component to the En–Jd garnets seems to stabilize the garnet phase at much lower pressures, thus approaching solubilities predicted by complete disorder of cations on all cubic and octahedral sites. On the other hand, the En–NaPx solvus indicates that the intermediate En–NaPx garnets have a higher degree of order than the En–Py garnets; this could be due to positional ordering of magnesium and sodium on the cubic subsites.

The experimental results presented here can be used to evaluate the possibility of a sharp phase transition in mantle pyroxenes at 400 km depth, corresponding to 130 kbar pressure. A univariant pyroxene-garnet transition, potentially responsible for the 400 km discontinuity, is present in several pyroxene systems: En, En–Di, En–Jd, En–NaPx and En–Di–Jd. In the En–Di–Jd system, the first garnet appears at 133 kbar, 1650° C; thus, the univariant formation of this garnet from a two-pyroxene assemblage could produce a sharp discontinuity at pressures corresponding to 400 km depth. However, such transition would also require the mantle compositions to be limited to the tie line between the composition of the first garnet ($En_{42}Di_9Jd_{49}$) and enstatite. A two-pyroxene assemblage of any other ternary bulk composition would transform to garnet and some residual pyroxene over a pressure interval during which the garnet and the two pyroxenes are at equilibrium. Figure 16 shows, for example, the tie lines connecting hypothetical compositions of the three coexisting phases at 140 and 150 kbar. Between 133 and 140 kbar, the garnet stability field expands rapidly with pressure, and the transformation from a two-pyroxene assemblage to garnet and residual pyroxene could occur over a pressure interval of 0–3 kbar, which is still sufficiently narrow to satisfy the seismic observations of the 400 km discontinuity. Thus, the pyroxene-garnet transition could produce a sharp 400 km discontinuity for a wide range of mantle compositions.

An important limitation on the garnet compositions is the absence of the pyrope-grossular-almandine component, which would otherwise spread out the transition to lower pressures. In this sense, the phase relations in a multicomponent system closely resemble the phase relations on the enstatite-pyrope join, where a sharp transition is possible only for the enstatite endmember. The garnet could lack the pyrope-grossular-almandine component, if the earth's mantle in the vicinity of the 400 km discontinuity formed originally as a pyroxene residue, and at high enough pressures to produce pyroxenes with negligible tetrahedral aluminum.

Acknowledgements. I am grateful to S.R. Bohlen, C.T. Herzberg and R.C. Liebermann for the reviews. This study was funded by a National Science Foundation grant EAR 86-17550 to the author. The high pressure experiments reported in this paper were performed in the Stony Brook High Pressure Laboratory which is jointly supported by the National Science Foundation Division of Earth Sciences (EAR 86-07105) and the State University of New York at Stony Brook.

References

Akaogi M, Akimoto S (1977) Pyroxene-garnet solid-solution equilibria in the systems $Mg_4Si_4O_{12}-Mg_3Al_2Si_3O_{12}$ and $Fe_4Si_4O_{12}-Fe_3Al_2Si_3O_{12}$ at high pressures and temperatures. Phys Earth Planet Int 15:90–106

Akaogi M, Ross NL, McMillan P, Navrotsky A (1984) The Mg_2SiO_4 polymorphs (olivine, modified spinel and spinel) – thermodynamic properties from oxide melt solution calorimetry, phase relations, and models of lattice vibrations. Am Mineral 69:499–512

Akaogi M, Navrotsky A, Yagi T, Akimoto S (1987) Pyroxene-garnet transformation: thermochemistry and elasticity of garnet solid solutions, and application to a pyrolite mantle. In: Manghnani MH, Syono Y (eds) High-pressure research in mineral physics. Terrapub, Tokyo, pp 251–260

Akimoto S, Yagi T, Inoue K, Sato Y (1975) High-pressure X-ray diffraction study on barium up to 130 kbar. High Temp High Pressures 7:287–294

Angel RJ, Gasparik T, Ross NL, Finger LW, Prewitt CT, Hazen RM (1988) A silica-rich sodium pyroxene phase with six-coordinated silicon. Nature 335:156–158

Anderson DL, Bass JD (1986) Transition region of the Earth's upper mantle. Nature 320:321–328

Block S (1978) Round-robin study of the high pressure phase transition in ZnS. Acta Cryst A 34, Suppl 316

Boyd FR, England JL (1960) Apparatus for phase-equilibrium measurements at pressures up to 50 kilobars and temperatures up to 1750° C. J Geophys Res 65:741–748

Carlson WD, Lindsley DH (1988) Thermochemistry of pyroxenes on the join $Mg_2Si_2O_6-CaMgSi_2O_6$. Am Mineral 73:242–252

Gasparik T (1985) Experimental study of subsolidus phase relations and mixing properties of pyroxene and plagioclase in the system $Na_2O-CaO-Al_2O_3-SiO_2$. Contrib Mineral Petrol 89:346–357

Gasparik T (1986) The compositions of coexisting clinopyroxene and orthopyroxene on the enstatite-jadeite join. EOS 67:368

Gasparik T (1987) The enstatite-jadeite solvus at 140 kbar. EOS 68:432

Gasparik T (1988) The synthesis of a new pyroxene-$NaMg_{0.5}Si_{2.5}O_6$ and garnet near the diopside-jadeite join. EOS 69:500

Gasparik T, Newton RC (1984) The reversed alumina contents of orthopyroxene in equilibrium with spinel and forsterite in the system $MgO-Al_2O_3-SiO_2$. Contrib Mineral Petrol 85:186–196

Guggenheim EA (1967) Thermodynamics. North-Holland Publishing Company, Amsterdam, pp 390

Gwanmesia GD (1987) Pressure calibration in a girdle-anvil and a DIA-type high pressure apparati at room temperature (25° C) and high temperature (1000° C). Master Thesis, State University of New York at Stony Brook

Herzberg CT, O'Hara MJ (1985) Origin of mantle peridotite and komatiite by partial melting. Geophys Res Lett 12:541–544

Howells S, O'Hara MJ (1978) Low solubility of alumina in enstatite and uncertainties in estimated paleogeotherms. Phil Trans R Soc Lond A 288:471–486

Irifune T, Sekine T, Ringwood AE, Hibberson WO (1986) The eclogite-garnetite transformation at high pressure and some geophysical implications. Earth Planet Sci Lett 77:245–256

Irifune T, Susaki J, Yagi T, Sawamoto H (1989) Phase transformations in diopside $CaMgSi_2O_6$ at pressures up to 25 GPa. Geophys Res Lett 16:187–190

Ito E, Takahashi E (1987) Ultrahigh pressure phase transformations and the constitution of the deep mantle. In: Manghnani MH, Syono Y (eds) High pressure research in mineral physics. Terrapub, Tokyo, pp 221–229

Ito E, Takahashi E (1988) Post-spinel transformations in the system $Mg_2SiO_4-Fe_2SiO_4$. Abstr 29th High Pressure Conf Jpn, 254–255

Kanzaki M (1987) Ultrahigh-pressure phase relations in the system $Mg_4Si_4O_{12}-Mg_3Al_2Si_3O_{12}$. Phys Earth Planet Int 49:168–175

Kato T, Kumazawa M (1985) Garnet phase of $MgSiO_3$ filling the pyroxene-ilmenite gap at very high temperature. Nature 316:803–805

Katsura T (1988) The system $Mg_2SiO_4-Fe_2SiO_4$ at high temperatures and high pressures. Abstr 29th High Pressure Conf Jpn, 256–257

Kushiro I (1965) Coexistence of nepheline and enstatite at high pressures. Carnegie Inst Wash Yearb 64:109–112

Lindsley DH, Grover JE, Davidson PM (1981) The thermodynamics of the $Mg_2Si_2O_6-CaMgSi_2O_6$ join: a review and an improved model. In: Newton RC, Navrotsky A, Wood BJ (eds) Advances in physical geochemistry, vol 1. Thermodynamics of minerals and melts. Springer, New York Berlin Heidelberg, pp 149–175

Liu L (1977) The system enstatite-pyrope at high pressures and temperatures and the mineralogy of the earth's mantle. Earth Planet Sci Lett 36:237–245

Liu L (1982) Chemical inhomogeneity of the mantle: geochemical considerations. Geophys Res Lett 9:124–126

Liu L (1987) New silicate perovskites. Geophys Res Lett 14:1079–1082

Lloyd EC (1971) Accurate characterization of the high pressure environment. NBS Spec Publ No 326, Washington DC, pp 1–3

MacGregor ID (1974) The system $MgO-Al_2O_3-SiO_2$: Solubility of Al_2O_3 in enstatite for spinel and garnet peridotite compositions. Am Mineral 59:110–119

McMillan P, Akaogi M, Ohtani E, Williams Q, Nieman R, Sato R (1988) Cation disorder in majorite garnets: an infrared, Raman and NMR study. EOS 69:1435

Pacalo REG, Gasparik T (1989) Reversals of the orthoenstatite-clinoenstatite transition at high pressures and temperatures. EOS 70:508

Pierson ML, Windom KE (1986) Experimental determination of pyroxene compositions on the jadeite-enstatite join at 25 kbar pressure. GSA Abstr Progr 18:718

Presnall DC, Gasparik T (1989) Melting of enstatite from 10 to 16.5 GPa. EOS 70:483

Remsberg AR, Boland JN, Gasparik T, Liebermann RC (1988) Mechanism of the olivine-spinel transformation in Co_2SiO_4. Phys Chem Minerals 15:498–506

Ringwood AE (1967) The pyroxene-garnet transformation in the earth's mantle. Earth Planet Sci Lett 2:255–263

Ringwood AE, Major A (1966) High-pressure transformations in pyroxenes. Earth Planet Sci Lett 1:351–357

Ringwood AE, Major A (1971) Synthesis of majorite and other high pressure garnets and perovskites. Earth Planet Sci Lett 12:411–418

Ross NL, Navrotsky A (1988) Study of the $MgGeO_3$ polymorphs (orthopyroxene, clinopyroxene, and ilmenite structures) by calorimetry, spectroscopy, and phase equilibria. Am Mineral 73:1355–1365

Sawamoto H (1987) Phase diagram of $MgSiO_3$ at pressures up to 24 GPa and temperatures up to 2200° C: phase stability and properties of tetragonal garnet. In: Manghnani MH, Syono Y (eds) High-pressure research in mineral physics. Terrapub, Tokyo, pp 209–219

Sawamoto H, Kohzaki M (1985) Garnet-like $MgSiO_3$ and constitution of the upper mantle. The first USSR-Japan symposium on phase transformations at high pressures and high temperatures, Reports, pp 48–50

Sawamoto H, Weidner DJ, Sasaki S, Kumazawa M (1984) Single-crystal elastic properties of the modified spinel (beta) phase of magnesium orthosilicate. Science 224:749–751

Shannon RD, Prewitt CT (1970) Synthesis and structure of a new high-pressure form of Rh_2O_3. J Solid State Chem 2:134–136

Suzuki T, Yagi T, Akimoto S (1981) Precise determination of transition pressure of GaAs. Abstr 22nd High Pressure Conf Jpn, 8–9

Swanson DK, Prewitt CT (1983) The crystal structure of $K_2Si^{VI}Si_3^{IV}O_9$. Am Mineral 68:581–585

Takahashi E, Yamada H, Ito E (1982) An ultrahigh-pressure furnace assembly to 100 kbar and 1500° C with minimum temperature uncertainty. Geophys Res Lett 9: 805–807

Tamai H, Yagi T (1987) Phase transformations in $CaSiO_3$ and $CaMgSi_2O_6$ under high pressure. Abstr 28th High Pressure Conf Jpn, 130–131

Weidner DJ (1986) Mantle model based on measured physical properties of minerals. In: Saxena SK(ed) Chemistry and physics of terrestrial planets. Adv Phys Geochem 6. Springer, New York Berlin Heidelberg, pp 251–274

Windom KE, Unger CP (1988) Stability of the assemblage albite plus forsterite at high temperatures and pressures with petrologic implications. Contrib Mineral Petrol 98:390–400

Yagi T, Akimoto S (1976) Direct determination of coesite-stishovite transition by in-situ X-ray measurements. Tectonophys 35:259–270

Yamada H, Takahashi E (1984) Subsolidus phase relations between coexisting garnet and two pyroxenes at 50 to 100 kbar in the system $CaO-MgO-Al_2O_3-SiO_2$. In: Kornprobst J (ed) Kimberlites II: the mantle and crust-mantle relationships. Elsevier, Amsterdam, pp 247–255

Yoder HS Jr, Tilley CE (1962) Origin of basalt magmas: an experimental study of natural and synthetic rock systems. J Petrol 3:342–532

Received May 24, 1988 / Accepted March 16, 1989
Editorial responsibility: I.S.E. Carmichael